Density jump as a function of the field for parallel relativistic collisionless shocks

Antoine Bret[1,2] and Ramesh Narayan[3,4]

[1]ETSI Industriales, Universidad de Castilla-La Mancha, Ciudad Real 13071, Spain
[2]Instituto de Investigaciones Energéticas y Aplicaciones Industriales, Campus Universitario de Ciudad Real, Ciudad Real 13071, Spain
[3]Center for Astrophysics – Harvard & Smithsonian, Harvard University, 60 Garden St., Cambridge, MA 02138, USA
[4]Black Hole Initiative at Harvard University, 20 Garden St., Cambridge, MA 02138, USA

Corresponding author: Antoine Bret, antoineclaude.bret@uclm.es

Collisionless shocks are frequently analysed using the magnetohydrodynamic (MHD) formalism, even though the required collisionality hypothesis is not fulfilled. In a previous work (Bret & Narayan, 2018 *J. Plasma Phys.* vol. **84**, p. 905840604), we presented a model of collisionless shock displaying an important departure from the expected MHD behaviour, in the case of a strong flow aligned magnetic field. This model was non-relativistic. Here, it is extended to the relativistic regime, considering zero upstream pressure and upstream Lorentz factor $\gg 1$. The result agrees satisfactorily with Particle-in-Cell simulations and shows a similar, and important, departure from the MHD prediction. In the strong field regime, the density jump r, seen in the downstream frame, behaves like $r \sim 2 + 1/\gamma_{\mathrm{up}}$, while MHD predicts 4 ($\gamma_{\mathrm{up}}$ is the Lorentz factor of the upstream measured in the downstream frame). Only pair plasmas are considered.

Key words: astrophysical Plasmas, plasma nonlinear Phenomena, space plasma Physics

---

1. Introduction

Shock waves are fundamental phenomena in fluids. In an electrically neutral medium, only binary collisions can mediate the transition between the upstream and the downstream. Consequently, the width of the shock front is of the order of a few mean free paths (Zel'dovich & Raizer 2002). In a plasma where the mean free path is greater than the dimensions of the system, shock waves can also propagate, mediated by collective electromagnetic effects (Sagdeev 1966). Such shock waves are called 'collisionless shocks'.

When it comes to analysing such shocks, the jump equations of magnetohydrodynamics (MHD) are frequently used, even though this formalism assumes a small mean path since it ultimately relies on fluid mechanics. It is therefore important to know to what extent the use of MHD is legitimate, or not, when it comes to analysing collisionless shocks.
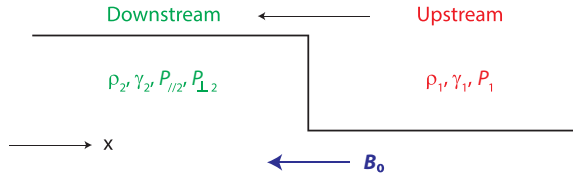
FIGURE 1. Densities ρ_i and pressures P_i are measured in the fluids (upstream and downstream) rest frame. Lorenz factors γ_i are measured in the front frame. The upstream is assumed isotropic, but not the downstream. Only the case of a strong shock, namely $P_1 = 0$ (sonic Mach number $M_s = \infty$) and $\gamma_1 \gg 1$, is studied in this work.

We previously (Bret & Narayan 2018) developed a model capable of predicting the density jump of a collisionless shock in the presence of a parallel magnetic field. The interest of this set-up is that according to MHD, the magnetic field should play no role in the density jump of a parallel shock (Kulsrud 2005). However, our model showed that for a strong enough field, the density jump of a strong sonic shock can go from 4 to 2. This theory has been validated by Particle-in-Cell (PIC) simulations by Haggerty, Bret & Caprioli (2022).

The model of Bret & Narayan (2018) was non-relativistic. However, even in the relativistic case, a sharp reduction in the density jump, compared with MHD predictions, was also observed by Bret *et al*. (2017).

The aim of the present work is to develop the relativistic version of the theory described by Bret & Narayan (2018), and compare the result with the PIC simulations of Bret *et al*. (2017).

In the non-relativistic regime, in line with Buckingham's π theorem (Buckingham 1914), the number of parameters and basic units allows to compute the density jump in terms of two dimensionless parameters only: the upstream sonic Mach number M_s and the magnetic parameters σ, defined later by (3.5).[1] In the present relativistic regime, the speed of light is added to the list of parameters. Conversely, the problem must be solved in terms of $2 + 1$ dimensionless parameters: M_s, σ and γ_1, the upstream Lorentz factor. In the following, we shall only consider the strong sonic shock case, namely $M_s = \infty$, having only σ and γ_1 left as free parameters.

Since the non-relativistic limit has been dealt with by Bret & Narayan (2018), we shall here only explore the regime $\gamma_1 \gg 1$.

Sections 2 and 3 summarise the physics of the theory and the relativistic conservation equations needed. Then, the problem is solved in §§ 4–6, in the front frame. Yet, because the PIC simulations were performed in the downstream frame, our solution must be boosted to this frame. This is achieved in § 7.

2. Method

For the present work to be self-contained, the method described by Bret & Narayan (2018) is recalled.

The basic idea is that as the upstream plasma goes through the front, it undergoes an anisotropic compression: it is mainly compressed in the direction parallel to the motion. The resulting downstream is therefore anisotropic, with an increased

---

[1]Five parameters (ρ_1, v_1, P_1, B_0, q), where q is the elementary charge. Three basic units (m, kg, s); hence, $5 - 3 = 2$ dimensionless parameters governing the problem.

temperature perpendicular to the motion and the field, while the perpendicular temperature has been conserved.

This stage of the downstream is called 'Stage 1'. In a collisional fluid, binary collisions would quickly restore isotropy on a time scale given by the collision frequency. In a non-magnetised collisionless medium, the Weibel instability would also restore isotropy, on a time scale given by the growth rate (Weibel 1959; Silva, Afeyan & Silva 2021). However, in the presence of an ambient magnetic field, both theory and solar wind observations show that an anisotropy can definitely be stable (Gary 1993; Bale *et al*. 2009; Maruca, Kasper & Bale 2011). This is the very reason why the behaviour of a collisionless shock can differ from its fluid counterpart. Note that shock accelerated particles, neglected here, can also trigger a departure from MHD (Bret 2020; Haggerty & Caprioli 2020).

If the field is strong enough to stabilise it, then Stage 1 is the end state of the downstream. In contrast, the plasma migrates to the instability threshold,[2] namely, by definition 'Stage 2'.

Whether we characterise Stage 1 or 2, the density jump is computed from the anisotropic MHD equations (Hudson 1970). Yet, within these equations, the anisotropy degree of the downstream is left as a free parameter. The process previously described specifically aims at determining this parameter. More precisely, there are three MHD jump equations for the parallel case. However, the downstream state involves four unknowns.[3] Therefore, an additional equation is needed to solve the problem. For Stage 1, this missing equation is simply $T_{\perp 2} = T_{\perp 1}$. For Stage 2, the marginal stability requirement provides the missing equation.

The formalism was developed for a pair plasma. It enables consideration of only one single parallel temperature and one single perpendicular temperature instead of four different temperature parameters for ions and electrons, as species of different mass can be heated differently at the front crossing (Guo *et al*. 2017, 2018). Yet, our strategy eventually relies mainly on the macroscopic MHD formalism. This enables the thought that it could be extended unchanged to electron/ion plasmas, only rescaling some dimensionless parameters. PIC simulations are currently performed to confirm this point (Shalaby, Bret & Fraschetti 2025). Yet, in the present work, we shall stick to pair plasmas.

3. Conservation equations

For a parallel shock,[4] the relativistic conservation equations in the front frame have been derived by Double *et al*. (2004) and Gerbig & Schlickeiser (2011). They read

$$[\rho\gamma\beta] = 0,$$
$$[\gamma^2\beta(e + P_\parallel)] = 0,$$
$$[\gamma^2\beta^2(e + P_\parallel) + P_\parallel] = 0,$$
$$[B] = 0, \tag{3.1}$$

where e, ρ, P are the internal energy, the mass density, and the pressure of the upstream and downstream fluids in their rest frame. Here, γ is the Lorentz factor

[2]Firehose, see §4.1.
[3]See §3.
[4]See Kennel & Coroniti (1984) for a perpendicular shock.

of the fluid in the front frame and $\beta = \sqrt{1 + \gamma^{-2}}$. The last equation shows the field is conserved at the interface, as is the case for a non-relativistic system (Majorana & Anile 1987; Kulsrud 2005). We shall therefore drop it when writing these equations in the following. In addition, these equations imply that for such an orientation of the field, the MHD problem is eventually equivalent to the fluid problem.

The internal energy e for an anisotropic relativistic gas reads (Double *et al.* 2004; Gerbig & Schlickeiser 2011)

$$e = \frac{2P_\perp + P_\parallel}{3(\Gamma - 1)} + \rho c^2. \tag{3.2}$$

Strictly speaking, the adiabatic index Γ is a function of the upstream quantities since depending on them, the downstream can be relativistic in its rest frame, or not.[5] A non-relativistic downstream has $\Gamma = 5/3$, and $\Gamma = 4/3$ if it is relativistic. Because we here consider $\gamma_1 \gg 1$, we shall consider $\Gamma = 4/3$ in the following.

The first three equations contain four unknowns: ρ_2, γ_2, $P_{\parallel 2}$ and $P_{\perp 2}$. The Stage 1 and 2 constraints on $P_{\perp, \parallel 2}$ then provide the fourth equation allowing to solve the problem.

The problem will be dealt with in terms of the following dimensionless variables:

$$r = \frac{\rho_2}{\rho_1}, \tag{3.3}$$

$$\theta_{\perp, \parallel} = \frac{P_{\perp, \parallel}}{\rho_1 c^2}, \tag{3.4}$$

$$\sigma = \frac{B_0^2 / 4\pi}{\gamma_1 \rho_1 c^2}, \tag{3.5}$$

$$A_2 = \frac{P_{\perp 2}}{P_{\parallel 2}}, \tag{3.6}$$

which stand for the density ratio, the dimensionless pressures, the magnetic field parameter[6] and the downstream anisotropy, respectively.

Accounting for $P_1 = 0$, (3.1) reads

$$\rho_1 \gamma_1 \beta_1 = \rho_2 \gamma_2 \beta_2, \tag{3.7}$$

$$\gamma_1^2 \beta_1 = \gamma_2^2 \beta_2 \left(\frac{2\theta_{\perp 2} + \theta_{\parallel 2}}{3(\Gamma - 1)} + \frac{\rho_2}{\rho_1} + \theta_{\parallel 2} \right), \tag{3.8}$$
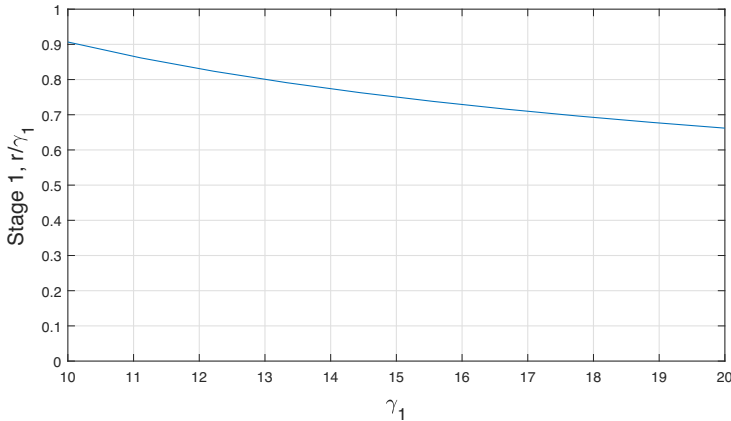
$$\gamma_1^2 \beta_1^2 = \gamma_2^2 \beta_2^2 \left(\frac{2\theta_{\perp 2} + \theta_{\parallel 2}}{3(\Gamma - 1)} + \frac{\rho_2}{\rho_1} + \theta_{\parallel 2} \right) + \theta_{\parallel 2}. \tag{3.9}$$

Using the first one to derive

$$r = \frac{\rho_2}{\rho_1} = \frac{\gamma_1 \beta_1}{\gamma_2 \beta_2}, \tag{3.10}$$

[5] With $P_1 = 0$, the adiabatic index of the upstream is not an issue.

[6] Although the field does not appear in the conservation equations, it does play a role in the analysis of Stage 2. See §5.

FIGURE 2. Density ratio for Stage 1, normalised to γ_1.

and using it to eliminate ρ_2 in the second and the third, we obtain the system we shall solve for both Stage 1 and Stage 2,

$$\gamma_1^2 \beta_1 = \gamma_2^2 \beta_2 \left(\frac{2\theta_{\perp 2} + \theta_{\|2}}{3(\Gamma - 1)} + \frac{\gamma_1 \beta_1}{\gamma_2 \beta_2} + \theta_{\|2} \right), \tag{3.11}$$

$$\gamma_1^2 \beta_1^2 = \gamma_2^2 \beta_2^2 \left(\frac{2\theta_{\perp 2} + \theta_{\|2}}{3(\Gamma - 1)} + \frac{\gamma_1 \beta_1}{\gamma_2 \beta_2} + \theta_{\|2} \right) + \theta_{\|2}. \tag{3.12}$$

4. Stage 1

Here, we assume $T_\perp$ is conserved, so that $T_{\perp 2} = T_{\perp 1} = 0$. We therefore set $\theta_{\perp 2} = 0$ in (3.11) and (3.12). Eliminating $\theta_{\|2}$ between (3.11) and (3.12) gives the equation for β_2,

$$(3\Gamma - 2)\gamma_1 \gamma_2^2 \beta_2 (\beta_2 - \beta_1) + 3(\Gamma - 1)(\gamma_1 - \gamma_2) = 0. \tag{4.1}$$

Considering in addition $\beta_1 \sim 1$ and $\Gamma = 4/3$, it simplifies to

$$\sqrt{1 - \beta_2^2} - (\beta_2 - 1)^2 \gamma_1 = 0. \tag{4.2}$$

Equation (3.3) then gives the density ratio for Stage 1,

$$r S1 \equiv \frac{\rho_2}{\rho_1} = \frac{\gamma_1 \beta_1}{\gamma_2 \beta_2} \sim \frac{\gamma_1}{\gamma_2 \beta_2}, \tag{4.3}$$

We plot in figure 2 the quantity $r S1/\gamma_1$ for a direct comparison with the isotropic case (see Appendix A), namely,

$$\left. \frac{\rho_2}{\rho_1} \right|_{\text{Iso}} = 2^{3/2} \gamma_1 \sim 2.82 \gamma_1. \tag{4.4}$$

With $\gamma_1 \gg 1$, we find the expansion

$$r S1 = (2\gamma_1)^{2/3} + \mathcal{O}(1). \tag{4.5}$$

FIGURE 3. Stability diagram of Stage 1. Since $T_{\perp 2} = 0$, it lies on the red line and is firehose stable within the shaded area.

4.1. *Stability of Stage* 1

Since $T_{\|2} \neq 0$ while $T_{\perp 2} = 0$, the downstream anisotropy parameter in Stage 1 is

$$A_2 = \frac{P_{\perp 2}}{P_{\|2}} = 0. \tag{4.6}$$

As is the case for the non-relativistic system, Stage 1 can therefore be firehose unstable. The threshold of this instability is the same for the relativistic case than for the non-relativistic one (Noerdlinger & Yui 1968; Barnes & Scargle 1973), that is,

$$A_2 = 1 - \frac{1}{\beta_{p\|2}}, \tag{4.7}$$

where[7]

$$\beta_{p\|2} = \frac{P_{\|2}}{B_0^2/4\pi}. \tag{4.8}$$

The stability diagram so defined is pictured in figure 3. With $T_{\perp 2} = 0$, Stage 1 lies on the red line. It is firehose stable for $\beta_{p\|2} \leq 1$, that is,

$$P_{\|2} \leq \frac{B_0^2}{4\pi}. \tag{4.9}$$

Using the dimensionless field parameter (3.5), criteria (4.7) reads

$$\frac{\theta_{\perp 2}}{\theta_{\|2}} = 1 - \gamma_1 \frac{\sigma}{\theta_{\|2}}. \tag{4.10}$$

Solving the right-hand side $= 0$, that is,

$$\gamma_1 \sigma_c \equiv \theta_{\|2}, \tag{4.11}$$

---

[7]The notation $\beta_{p\|2}$ has been chosen to clearly distinguish this magnetisation parameter from the downstream parameter $\beta_2 = v_2/c$.

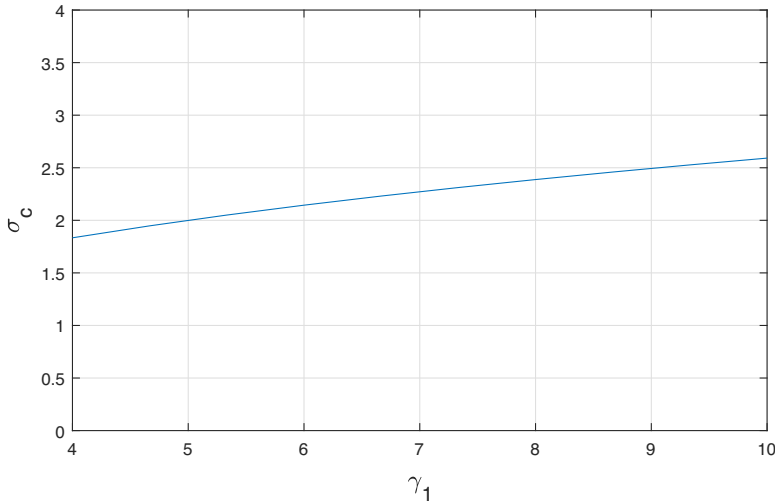FIGURE 4. Critical value σ_c of σ defined by (4.13), above which the magnetic field stabilises Stage 1.

allows to define σ_c, the critical σ below which Stage 1 is unstable. To this extent, the value of $\theta_{\|2}$ is extracted from (3.11). With $\theta_{\perp 2} = 0$, and accounting for $\Gamma = 4/3$ and $\beta_1 \sim 1$, it reads

$$\theta_{\|2} = \frac{\gamma_1}{\gamma_2} \frac{\gamma_1 - \gamma_2}{2\beta_2\gamma_2}. \tag{4.12}$$

Substituting in (4.11) then gives

$$\sigma_c = \frac{\gamma_1(1 - \beta_2^2) - \sqrt{1 - \beta_2^2}}{2\beta_2} = \gamma_1(1 - \beta_2), \tag{4.13}$$

where β_2 is function of γ_1 via (4.2). Figure 4 shows σ_c plotted in terms of γ_1.

For $\gamma_1 \gg 1$, we find the expansion

$$\sigma_c = (2\gamma_1)^{1/3} + \mathcal{O}(\gamma_1^{-1/3}). \tag{4.14}$$

As the upstream kinetic energy grows, it takes an increasing field to stabilise Stage 1.

5. Stage 2

We need now assess the end state of the downstream in case Stage 1 is unstable, namely, Stage 2. To do so, we come back to (3.11) and (3.12), and add the marginal firehose stability requirement (4.10). The resolution follows the following lines.

(i) Use (4.10) to express $\theta_{\|2}$ in terms of $\theta_{\perp 2}$ and σ, namely,

$$\theta_{\|2} = \theta_{\perp 2} + \gamma_1\sigma. \tag{5.1}$$

(ii) Replace the resulting expression of $\theta_{\|2}$ in (3.11) and (3.12), which gives

$$\beta_2\gamma_2^2 \left(\frac{\gamma_1}{\beta_2\gamma_2} + 2(\gamma_1\sigma + \theta_{\perp 2}) + 2\theta_{\perp 2} \right) - \gamma_1^2 = 0, \tag{5.2}$$

$$\beta_2^2\gamma_2^2 \left(\frac{\gamma_1}{\beta_2\gamma_2} + 2(\gamma_1\sigma + \theta_{\perp 2}) + 2\theta_{\perp 2} \right) - \gamma_1^2 + \gamma_1\sigma + \theta_{\perp 2} = 0. \tag{5.3}$$
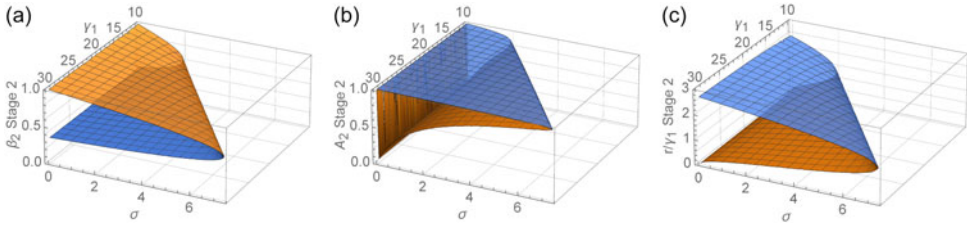
FIGURE 5. Solutions of (3.11), (3.12) and (4.10) for (*a*) β_2, (*b*) A_2 and (*c*) r/γ_1 in Stage 2. The blue branch is the physical one as its r/γ_1 merges with the fluid result for $\sigma = 0$ (i.e. $r/\gamma_1 = 2^{3/2} \sim 2.82$). The lower branch in panel (*c*), the orange one, starts from $r < 1$.

(iii) Then, eliminate $\theta_{\perp 2}$ between these two equations.

For $\gamma = 4/3$ and $\gamma_1 \gg 1$, we eventually obtain an equation for β_2 only,

$$\sqrt{1 - \beta_2^2} + \gamma_1(4\beta_2 - 3\beta_2^2 - 1) = 2\beta_2\sigma. \tag{5.4}$$

The downstream anisotropy is then computed as

$$A_2 = \gamma_1 \frac{-\beta_2^3 + \beta_2 + \beta_2^2 \Omega(\gamma_1 + \sigma) + \Omega(\sigma - \gamma_1)}{\Omega\sigma\left(\beta_2^2(\gamma_1 - 3) + \gamma_1 - 1\right) - \left(\beta_2^2 - 1\right)\gamma_1(\beta_2 - \Omega\gamma_1)}, \tag{5.5}$$

with $\Omega = \sqrt{1 - \beta_2^2}$. It is easily checked that $A_2 = 1$ for $\sigma = 0$.

Figure 5 displays the β_2 solutions of (5.4), A_2 given by (5.5) and r/γ_1 given by (3.10), in terms of (σ, γ_1). Because (5.4) gives two branches for β_2, A_2 and r/γ_1 display two branches as well. Figure 5(*c*) shows that only the upper branch, the blue one, merges with the fluid result for $\sigma = 0$ (i.e. $r/\gamma_1 = 2^{3/2} \sim 2.82$). In contrast, the lower branch, the orange one, starts from $r < 1$, a non-physical result. Therefore, the branch we need to consider is the blue one in panel (*c*), that is, the lower one in the β_2 plot.

Figure 6 shows a cut of figure 5(*b*) for $\gamma_1 = 10$. While it obviously goes to unity for $\sigma = 0$, it never goes to 0 on any branch. Indeed, it hardly goes down to 0.8 with the blue branch, namely, the physical one. In other words, our model does not allow for Stage 2 solutions down to $A_2 = 0$, where it would merge with Stage 1.

Noteworthily, the non-relativistic result of Bret & Narayan (2018) displayed a continuous transition between Stages 1 and 2, but only for a strong sonic shock.[8]

6. Putting Stages 1 and 2 together

We can now put Stages 1 and 2 together, to offer a complete solution, in the front frame, for the density jump and any $(\gamma_1 \gg 1, \sigma)$.

Because in our scenario, the plasma goes first to Stage 1, Stage 1 is the end state of the downstream as long as it is stable. The function $r(\sigma)$ is therefore defined by Stage 1 for $\sigma > \sigma_c$. If $\sigma < \sigma_c$, then the downstream settles in Stage 2, which therefore defines the density ratio. Hence,

$$r(\sigma) = \begin{cases} \text{Stage 2}, & \sigma < \sigma_c, \quad \text{Figure 5}, \\ \text{Stage 1}, & \sigma > \sigma_c, \quad \text{Figure 2}. \end{cases} \tag{6.1}$$
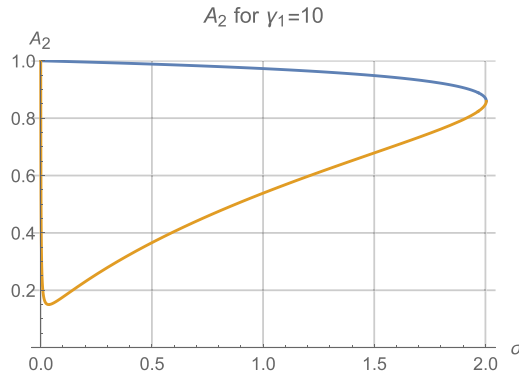
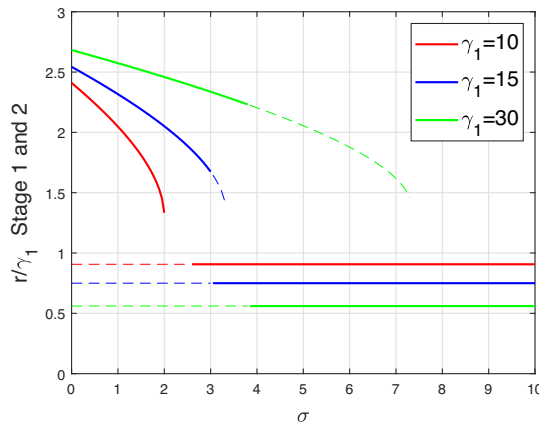[8]See Figure 5 of Bret & Narayan (2018).

FIGURE 6. Cut of figure 5(*b*) for $\gamma_1 = 10$.

FIGURE 7. Function $r(\sigma)/\gamma_1$ defined by (6.1) for three values of γ_1. The horizonal lines pertain to Stage 1, where the density ratio does not depend on σ. The dashed lines picture the Stage 1 or 2 solutions which are not relevant because Stage 1 is stable, or not.

Figure 7 displays the result. We plotted the function $r(\sigma)$ defined previously for three values of γ_1. The horizonal lines pertain to Stage 1, where the density ratio does not depend on σ. The dashed lines picture the Stage 1 or 2 solutions which are not relevant because Stage 1 is stable, or not. For $\gamma_1 = 15$ and 30, Stage 2 picks up (in terms of σ), when Stage 1 becomes unstable. For $\gamma_1 = 10$, Stage 2 does not offer solutions up to σ_c, which is why there is a σ-gap without solution for $\sigma \in [2, 2.6]$. Such has also been found to be the case for some oblique orientations of the field in the non-relativistic regime (Bret & Narayan 2022; Bret, Haggerty & Narayan 2024).

7. Switching to the downstream frame and comparison with 2-D3V PICs

The PIC simulations of Bret *et al.* (2017) were performed using the code TRISTAN-MP (Spitkovsky 2005). It is a parallel version of the code TRISTAN (Buneman 1993) optimised to study collisionless shocks. The spatial computational domain was two-dimensional (2-D), while the velocities and fields were rendered in

three dimensions. The simulations implemented the 'mirror' method, sending a cold $(k_B T \ll mc^2)$ relativistic pair plasma towards a reflecting wall. Since the shock is formed from the reflected part of the plasma interacting with the incoming part, the simulation was eventually performed in the shock downstream.

The simulation box was rectangular in the x, y plane, with periodic boundary conditions in the y direction and x direction of the flow. Each simulation cell was initialised with 16 electrons and 16 positrons. The time step of the simulations was $\Delta t = 0.045\omega_p^{-1}$, with $\omega_p^2 = 4\pi n_0 q^2 / \gamma_{1,df} m$, where n_0 is the incoming plasma density in its own frame, and m, q the electron mass and charge, respectively. The plasma skin depth c/ω_p was resolved with 10 simulation cells. The computational domain was $\sim 102 c/\omega_p$ in the y direction and $3600 c/\omega_p$ in the x direction, that is, approximately 36 000 cells long. Simulations typically extended up to $t = 3600\omega_p^{-1}$.

In (3.1), all fluid quantities are defined in their own rest frame. In turn, the Lorentz and β factors are measured in the front frame. Yet, the 2-D3V PIC simulations of Bret *et al.* (2017) were performed in the downstream frame. Therefore, we need to boost figure 7 to the downstream frame for a comparison with simulations.

A key quantity in this respect is $\gamma_{1,df}$, the Lorentz factor of the upstream seen from the downstream. With

$$\beta_{1,df} = \frac{\beta_1 - \beta_2}{1 - \beta_1 \beta_2}, \tag{7.1}$$

it reads

$$\gamma_{1,df} = \frac{1}{\sqrt{1 - \beta_{1,df}^2}} = \gamma_1 \gamma_2 (1 - \beta_1 \beta_2), \tag{7.2}$$

where the subscript df stands for 'downstream frame'.

Boosting figure 7 to the downstream frame implies boosting the density ratio, the σ parameter and the γ_1 parameter.

(i) Regarding the density ratio, we have

$$r_{df} = \frac{\rho_{2,df}}{\rho_{1,df}}. \tag{7.3}$$

Now, $\rho_{2,df}$ is simply ρ_2 since it is the downstream density in its own rest frame. Regarding $\rho_{1,df}$, it reads $\rho_{2,df} = \gamma_{1,df} \rho_1$. Therefore, and still for $\gamma_1 \gg 1$,

$$r_{df} = \frac{\rho_{2,df}}{\rho_{1,df}} = \frac{\rho_2}{\gamma_{1,df} \rho_1} = \frac{1}{\gamma_{1,df}} \frac{\gamma_1 \beta_1}{\gamma_2 \beta_2} \sim 1 + \frac{1}{\beta_2}. \tag{7.4}$$

Hence,

$$r_{df} = \begin{cases} 1 + 1/\beta_{2,S2}, & \sigma < \sigma_c, \\ 1 + 1/\beta_{2,S1}, & \sigma > \sigma_c, \end{cases} \tag{7.5}$$

where $\beta_{2,S1,S2}$ is β_2 in Stage 1 and 2, given by (4.2) and (5.4), respectively.

(ii) The σ parameter also needs a boost. In (3.5), the field remains unchanged since it is parallel to the boost. Only ρ_1 and γ_1 are modified. With $\rho_{1,df} = \gamma_{1,df} \rho_1$, we find

$$\sigma_{df} = \frac{B_0^2/4\pi}{\gamma_{1,df} \rho_{1,df} c^2} = \frac{\sigma}{\gamma_1 \gamma_2^2 (1 - \beta_1 \beta_2)^2} \sim \frac{\sigma}{\gamma_1 \gamma_2^2 (1 - \beta_2)^2} = \frac{1 + \beta_2}{1 - \beta_2} \frac{\sigma}{\gamma_1}. \tag{7.6}$$

In this σ re-scaling, β_2 is given by its Stage 1 expression when considering Stage 1, and by its Stage 2 expression when considering Stage 2.

With respect to the critical σ_c of σ below which Stage 1 is unstable, it reads, according to (4.13), $\sigma_c = \gamma_1(1 - \beta_2)$. Using (7.6), we obtain its value in the downstream frame,

$$\sigma_{c,df} = 1 + \beta_2, \tag{7.7}$$

where β_2 must be given by its Stage 1 expression since it defines the stability threshold for Stage 1. Therefore, the transition from Stage 1 to Stage 2, seen from the downstream frame, always occurs for $\sigma_{c,df} \in [1, 2]$.

(iii) Finally, the PIC simulations presented by Bret *et al.* (2017) considered two values for the upstream Lorentz factors, 10 and 30, defined in the downstream frame. In other words, simulations varying σ_{df} were performed at constant $\gamma_{1,df}$. It means that to match a PIC ran at $\gamma_{1,\text{PIC}}$, we need to run the abovementioned calculations for σ and γ_1, fulfilling

$$\gamma_{1,df} = \gamma_1 \gamma_2 (1 - \beta_2) = \gamma_{1,\text{PIC}}, \tag{7.8}$$

where we used $\beta_1 \sim 1$. Figure 8 shows the value of $\gamma_{1,df}$ in terms of (σ, γ_1), for Stages 1 and 2. Superimposed are the contours of constant $\gamma_{1,df} = 10$ and 30. They are flat for Stage 1, where $\gamma_{1,df}$ is independent of σ, and slightly bent upwards for Stage 2. As a result, we find the following correspondence.
In Stage 1,

$$\begin{aligned} \gamma_{1,df} = 10 &\Rightarrow \gamma_1 = 43, \\ \gamma_{1,df} = 30 &\Rightarrow \gamma_1 = 230. \end{aligned} \tag{7.9}$$

In Stage 2,

$$\begin{aligned} \gamma_{1,df} = 10 &\Rightarrow \gamma_1 \sim 16, \\ \gamma_{1,df} = 30 &\Rightarrow \gamma_1 \sim 43. \end{aligned} \tag{7.10}$$

It has been checked that for Stage 2, considering a constant γ_1 hardly affects the result.

With (7.2) reading $\gamma_{1,df} = \gamma_1 \gamma_2 (1 - \beta_1 \beta_2)$, one could expect in (7.9) for Stage 1, a value of γ_1 lower than 230. Indeed, if, as hinted in the Appendix, $\beta_2 \sim 1/3$ and $\gamma_2 \sim 1$, then with $\gamma_1 = 230$, $\gamma_{1,df} \sim 230 \times 1 \times 2/3 = 153 > 30$. However, in the present case, the value of β_2 has to be that derived in §4, for the anisotropic downstream in Stage 1, not the isotropic case treated in the Appendix. Additionally, for $\gamma_1 = 230$, Stage 1 has $\beta_2 \sim 0.967$, which explains how the product $\gamma_1 \gamma_2 (1 - \beta_1 \beta_2)$ is reduced to just 30.

Figure 9 is the end result of this article. It displays the density ratio measured in the downstream frame, r_{df}, in terms of σ_{df}. The transition between the two stages occurs for the critical $\sigma_{c,df}$ given by (7.7). The squares shows the results of the PIC simulations performed by Bret *et al.* (2017).[9]

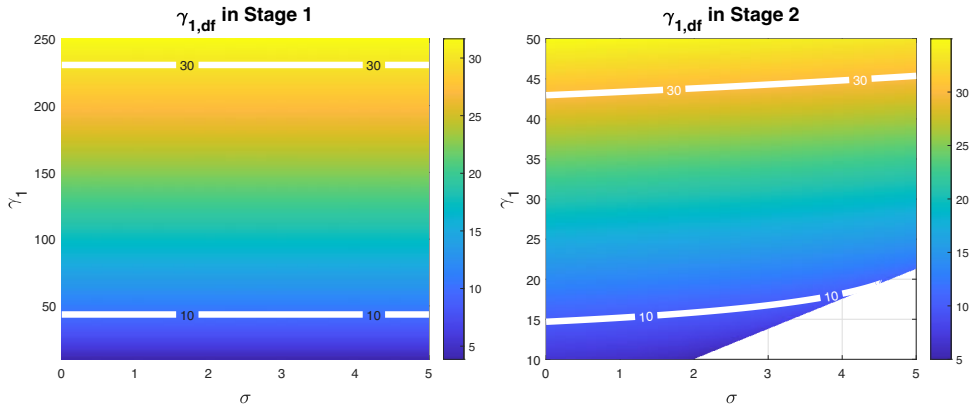---

[9]See Figures 3 and 6 of Bret *et al.* (2017).

FIGURE 8. Value of $\gamma_{1,df}$ in terms of (σ, γ_1), for Stages 1 and 2, with the contours of constant $\gamma_{1,df} = 10$ and 30.
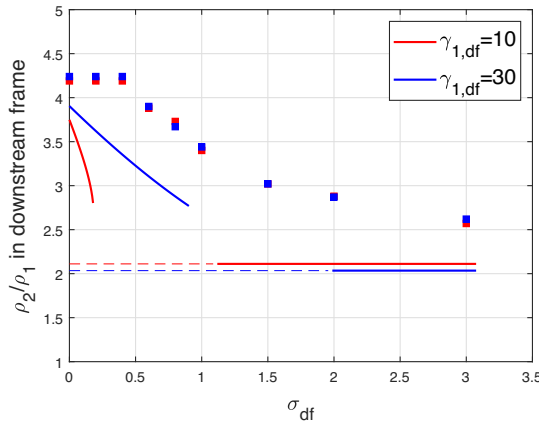

FIGURE 9. Density ratio measured in the downstream frame, r_{df}, in terms of σ_{df}. The transition between the two stages occurs for the critical $\sigma_{c,df}$ given by (7.7). The squares show the results of the PIC simulations performed by Bret *et al.* (2017).

Note that Stage 1 always defines the density ratio for large fields $\sigma_{df} > \sigma_{c,df}$. It is therefore instructive to derive an expansion of (7.4) in Stage 1. We find

$$r_{df,S1} = 1 + \frac{1}{\beta_{2,S1}} = 2 + \left(\frac{\sqrt{2}}{\gamma_1}\right)^{2/3} + \mathcal{O}(\gamma_1^{-4/3})$$

$$= 2 + \frac{1}{\gamma_{1,\text{PIC}}} + \mathcal{O}(\gamma_{1,\text{PIC}}^{-2}). \tag{7.11}$$

8. Conclusion

In this work, we have implemented the relativistic version of the model presented by Bret & Narayan (2018). The system considered is a collisionless shock in pair plasma, with a parallel magnetic field. Since numerical simulations have been carried out by Bret *et al.* (2017), we are able to compare the results of the present theory with these simulations.

After adapting to the relativistic case the theory presented by Bret & Narayan (2018), and boosting the results to the downstream frame, we reach, in figure 9, the comparison of the relativistic theory with the PIC simulations.

The agreement is satisfactory. Our model reproduces the fall of the density ratio over the correct σ_{df} range, with an asymptotic value close to 2 in the strong field regime $\sigma_{df} > \sigma_{c,df}$.

We observe two kinds of discrepancies in figure 9, between the theory and the simulations. (i) There is a systematic underestimation of the density ratio of the theory with respect to simulations and (ii) the PIC simulations find solutions where the model does not offer any, like for $\sigma_{df} = 1.5$ with $\gamma_{1,df} = 30$. Let us briefly comment on each point.

(i) In the absence of a magnetic field, the density jump measured in the downstream is given by (see Appendix A)

$$r_{df} = \frac{\Gamma}{\Gamma - 1}. \tag{8.1}$$

For an adiabatic index $\Gamma = 4/3$, this gives $r_{df} = 4$. Yet, as seen in figure 9, PIC simulations for a weak field give a slightly higher value, $r_{df} \sim 4.3$. Such an overshoot could be interpreted as the PIC effectively simulating an adiabatic index $\Gamma = 1.3$, slightly lower than the fully relativistic $\Gamma = 4/3 \sim 1.33$ considered in the theory.[10] Yet, this solution seems improbable, for if the downstream were not fully relativistic in the simulation, its adiabatic index would rather lean towards a higher value, namely $\Gamma = 5/3 \sim 1.66$. Why, then, is the density ratio in the PIC simulations higher than (8.1) predicts? The most probable answer is related to accelerated particles. It has been known for long that collisionless shocks can accelerate particles (Blandford & Ostriker 1978). Additionally, it has been equally known for long than their effect on the shock is to raise the density ratio (Berezhko & Ellison 1999; Stockem *et al*. 2012). To date, this is the only known mechanism capable of raising the density ratio above its MHD value (see Bret (2020) and references therein). Therefore, strictly speaking, the PICs presented here are not a simulation of the theory, since the theory ignores particles acceleration, which simulations necessarily include. The PIC simulations eventually simulate the system discussed here, embedded in a bath of cosmic rays.

(ii) In addition to ignoring particle acceleration, other differences between the PIC simulations and the theory are noticeable. For example, figures 3(b), 4(b) and 6(b) of Bret *et al*. (2017) show that while the upstream temperature is nearly 0, the downstream is definitely anisotropic in the PIC simulations, but its perpendicular temperature is never 0, even in the strong field regime. This means that Stage 1, as described here, is not fully realised. Probably due to the influence of cosmic rays, the simulations do not stick to the present theory, even though they follow its trend. It is therefore not surprising that the simulations find downstream solutions even when our rigid, 'cosmic rays-less' theory does not allow any. Future work could focus on some detailed analysis of the particle distribution in the PIC. Yet, as mentioned, it could be challenging to run some PIC simulations cancelling the cosmic rays they necessarily produce.

---

[10]Setting $\Gamma = 1.3$ in (8.1) yields $r_{df} = 4.3$.

There is a striking similarity between the non-relativistic and relativistic theories. In the non-relativistic theory, the density jump in strong field tends to $r = 2$. This is an important departure from the MHD prediction, since the latter predicts a field-independent density jump for a parallel shock of $r = 4$ (strong sonic shock).

The same pattern is observed here. Relativistic MHD still predicts a field-independent density jump for this parallel geometry, which amounts to a density jump measured in the downstream $r_{df} \sim 4$. In contrast, the relativistic theory presented here, and confirmed by simulations, gives a density jump also tending towards $r_{df} = 2$.

It is likely that, as in the non-relativistic case (Bret & Narayan 2022; Bret *et al*. 2024), the departure from MHD is maximum for this obliquity of the magnetic field. This could be confirmed in future works.

Extending this work to finite upstream pressures would require modifying the left-hand sides of (3.8) and (3.9), before implementing similar calculations following the same road map. While this could be the goal of some future work, the result would probably be a lowering of the density ratio with diminishing sonic Mach number, as was observed in the non-relativistic case (Bret & Narayan 2018).

Declaration of interests

The authors report no conflict of interest.

Appendix A. Jump conditions for an isotropic fluid with $P_1 = 0$

Although the simple case of a relativistic shock in an isotropic fluid has been abundantly discussed in the literature (Taub 1948; Anile 1990; Landau & Lifshitz 2013), we here present a simple derivation of the jump conditions, for $P_1 = 0$ and $\gamma_1 \gg 1$, using the present notation (Narayan 2012).

We start from (3.7)–(3.9), where only $P_1 = 0$ has been assumed. Setting $\theta_{\perp 2} = \theta_{\parallel 2} = \theta_2$ to reflect isotropy gives

$$\rho_1 \gamma_1 \beta_1 = \rho_2 \gamma_2 \beta_2, \tag{A.1}$$

$$\gamma_1^2 \beta_1 = \gamma_2^2 \beta_2 \left(\frac{\Gamma}{\Gamma - 1} \theta_2 + \frac{\rho_2}{\rho_1} \right), \tag{A.2}$$

$$\gamma_1^2 \beta_1^2 = \gamma_2^2 \beta_2^2 \left(\frac{\Gamma}{\Gamma - 1} \theta_2 + \frac{\rho_2}{\rho_1} \right) + \theta_2. \tag{A.3}$$

Computing (A.3) $-\beta_2 \times$ (A.2) gives

$$\gamma_1^2 \beta_1 (\beta_1 - \beta_2) = \theta_2. \tag{A.4}$$

Using this expression for θ_2 in (A.2) gives

$$\gamma_1 - \gamma_2 = \frac{\Gamma}{\Gamma - 1} \gamma_1 \gamma_2^2 \beta_2 (\beta_1 - \beta_2). \tag{A.5}$$

Since $\gamma_1 \gg 1$, $\beta_1 \sim 1$. In addition, because the downstream has to be subsonic while the speed of sound in a relativistic gas is $c/\sqrt{3}$, we know $\beta_2 < 1/\sqrt{3}$. Hence, $\gamma_2 \sim 1$ so that $\gamma_1 \gg \gamma_2$. Equation (A.5) therefore simplifies to

$$\gamma_1 - \gamma_2 \sim \gamma_1$$
$$\sim \frac{\Gamma}{\Gamma - 1} \gamma_1 \gamma_2^2 \beta_2 (1 - \beta_2)$$
$$\Rightarrow \beta_2 = \Gamma - 1, \tag{A.6}$$

where $\gamma_2^2 = (1 - \beta_2^2)^{-1}$ and $\beta_1 \sim 1$ has been used. This expression for β_2 is identical to (16) of Kirk & Duffy (1999). Then,

$$\gamma_2 = \frac{1}{\sqrt{1 - \beta_2^2}} = \frac{1}{\sqrt{(2 - \Gamma)\Gamma}}, \tag{A.7}$$

and from (3.10),

$$r = \frac{\rho_2}{\rho_1} \sim \frac{\gamma_1}{\beta_2 \gamma_2} = \gamma_1 \frac{\sqrt{\Gamma(2 - \Gamma)}}{\Gamma}. \tag{A.8}$$

Finally,

$$\gamma_{1,df} \sim \gamma_1 (1 - \beta_2) = \gamma_1 \sqrt{\frac{2 - \Gamma}{\Gamma}} \tag{A.9}$$

and

$$r_{df} = \frac{r}{\gamma_{1,df}} = \frac{\Gamma}{\Gamma - 1}. \tag{A.10}$$

For $\Gamma = 4/3$, (A.8) and (A.10) give $r = 2^{3/2} \gamma_1$ and $r_{df} = 4$, respectively. Note that PIC simulations, where velocities are rendered in only two dimensions, give a density ratio of $r_{df} = 3$, corresponding to $\Gamma = 3/2$.

Bret *et al.* (2017) rendered velocities in three dimensions, as explained in § 7. If they had been rendered in 2-D, the density jump would have been 3. For a direct comparison of the 2-D and 3-D cases in PIC simulations, see figure 3 of Bret *et al.* (2014).

REFERENCES

ANILE, A.M. 1990 *Relativistic Fluids and Magneto-Fluids: With Applications in Astrophysics and Plasma Physics*. Cambridge University Press.

BALE, S.D., KASPER, J.C., HOWES, G.G., QUATAERT, E., SALEM, C. & SUNDKVIST, D. 2009 Magnetic fluctuation power near proton temperature anisotropy instability thresholds in the solar wind. *Phys. Rev. Lett.* **103**, 211101.

BARNES, A. & SCARGLE, J.D. 1973 Collisionless damping of hydromagnetic waves in relativistic plasma. Weak Landau damping. *Astrophys. J.* **184**, 251–270.

BEREZHKO, E.G. & ELLISON, D.C. 1999 A simple model of nonlinear diffusive shock acceleration. *Astrophys. J.* **526**, 385–399.

BLANDFORD, R.D. & OSTRIKER, J.P. 1978 Particle acceleration by astrophysical shocks. *Astrophys. J. Lett.* **221**, L29–L32.

BRET, A. 2020 Can we trust MHD jump conditions for collisionless shocks? *Astrophys. J.* **900**, 111.

BRET, A., HAGGERTY, C.C. & NARAYAN, R. 2024 Density jump for oblique collisionless shocks in pair plasmas: physical solutions. *J. Plasma Phys.* **90**, 905900213.

BRET, A. & NARAYAN, R. 2018 Density jump as a function of magnetic field strength for parallel collisionless shocks in pair plasmas. *J. Plasma Phys.* **84**, 905840604.

BRET, A. & NARAYAN, R. 2022 Density jump for oblique collisionless shocks in pair plasmas: allowed solutions. *J. Plasma Phys.* **88**, 905880615.

BRET, A., PE'ER, A., SIRONI, L., SADOWSKI, A. & NARAYAN, R. 2017 Kinetic inhibition of magnetohydrodynamics shocks in the vicinity of a parallel magnetic field. *J. Plasma Phys.* **83**, 715830201.

BRET, A., STOCKEM, A., NARAYAN, R. & SILVA, L.O. 2014 Collisionless weibel shocks: full formation mechanism and timing. *Phys. Plasmas* **21**, 072301.

BUCKINGHAM, E. 1914 On physically similar systems; illustrations of the use of dimensional equations. *Phys. Rev.* **4**, 345–376.

BUNEMAN, O. 1993 Tristan: the 3-D electromagnetic particle code. In *Computer Space Plasma Physics*, (ed. H. MATSUMOTO & Y. OMURA), pp. 67. Terra Scientific.

DOUBLE, G.P., BARING, M.G., JONES, F.C. & ELLISON, D.C. 2004 Magnetohydrodynamic jump conditions for oblique relativistic shocks with gyrotropic pressure. *Astrophys. J.* **600**, 485–500.

GARY, S.P. 1993 *Theory of Space Plasma Microinstabilities*. Cambridge University Press.

GERBIG, D. & SCHLICKEISER, R. 2011 Jump conditions for relativistic magnetohydrodynamic shocks in a gyrotropic plasma. *Astrophys. J.* **733**, 32.

GUO, X., SIRONI, L. & NARAYAN, R. 2017 Electron heating in low-Mach-number perpendicular shocks. I. Heating mechanism. *Astrophys. J.* **851**, 134.

GUO, X., SIRONI, L. & NARAYAN, R. 2018 Electron heating in low Mach number perpendicular shocks. II. Dependence on the pre-shock conditions. *Astrophys. J.* **858**, 95.

HAGGERTY, C.C., BRET, A. & CAPRIOLI, D. 2022 Kinetic simulations of strongly magnetized parallel shocks: deviations from MHD jump conditions. *Mon. Not. R. Astron. Soc.* **509**, 2084–2090.

HAGGERTY, C.C. & CAPRIOLI, D. 2020 Kinetic simulations of cosmic-ray-modified shocks. I. Hydrodynamics. *Astrophys. J.* **905**, 1.

HUDSON, P.D. 1970 Discontinuities in an anisotropic plasma and their identification in the solar wind. *Planet. Space Sci.* **18**, 1611–1622.

KENNEL, C.F. & CORONITI, F.V. 1984 Confinement of the Crab pulsar's wind by its supernova remnant. *Astrophys. J.* **283**, 694–709.

KIRK, J.G. & DUFFY, P. 1999 Particle acceleration and relativistic shocks. *J. Phys. G: Nucl. Part. Phys.* **25**, R163–R194.

KULSRUD, R.M. 2005 *Plasma Physics for Astrophysics*. Princeton Univ. Press.

LANDAU, L.D. & LIFSHITZ, E.M. 2013 *Fluid Mechanics*. Elsevier Science.

MAJORANA, A. & ANILE, A.M. 1987 Magnetoacoustic shock waves in a relativistic gas. *Phys. Fluids* **30**, 3045–3049.

MARUCA, B.A., KASPER, J.C. & BALE, S.D. 2011 What are the relative roles of heating and cooling in generating solar wind temperature anisotropies? *Phys. Rev. Lett.* **107**, 201101.

NARAYAN, R. 2012 Lecture notes on relativistic hydrodynamics. Unpublished.

NOERDLINGER, P.D. & YUI, A.K.-M. 1968 Persistence of the firehouse instability in highly relativistic plasmas. *Astrophys. J.* **151**, 901.

SAGDEEV, R.Z. 1966 Cooperative phenomena and shock waves in collisionless plasmas. *Rev. Plasma Phys.* **4**, 23.

SHALABY, M., BRET, A. & FRASCHETTI, F. 2025 Parallel Collisionless Shocks in strongly Magnetized Electron-Ion Plasma. I. Temperature anisotropies. ArXiv:2503.10758.

SILVA, T., AFEYAN, B. & SILVA, L.O. 2021 Weibel instability beyond bi-Maxwellian anisotropy. *Phys. Rev. E* **104**, 035201.

SPITKOVSKY, A. 2005 Simulations of relativistic collisionless shocks: shock structure and particle acceleration. In *Astrophysical Sources of High Energy Particles and Radiation*, (ed., T.Bulik, Rudak, B. & Madejski, G.), vol. 801, pp. 345–350. American Institute of Physics Conference Series.

STOCKEM, A., FIÚZA, F., FONSECA, R.A. & SILVA, L.O. 2012 The impact of kinetic effects on the properties of relativistic electron-positron shocks. *Plasma Phys. Control. Fusion* **54**, 125004.

TAUB, A.H. 1948 Relativistic Rankine-Hugoniot equations. *Phys. Rev.* **74**, 328–334.

WEIBEL, E.S. 1959 Spontaneously growing transverse waves in a plasma due to an anisotropic velocity distribution. *Phys. Rev. Lett.* **2**, 83–84.

ZEL'DOVICH, Y.B. & RAIZER, Y.P. 2002 *Physics of Shock Waves and High-Temperature Hydrodynamic Phenomena*. Dover Publications.